PHYSICAL REVIEW E **88**, 012109 (2013)

# Statistical mechanics of a neutral point-vortex gas at low energy

J. G. Esler,[*] T. L. Ashbee, and N. R. Mcdonald
*Department of Mathematics, University College London, London, United Kingdom*

(Received 11 October 2012; revised manuscript received 9 February 2013; published 9 July 2013)

The statistics of a neutral point-vortex gas in an arbitrary two-dimensional simply connected and bounded container are investigated in the framework of the microcanonical ensemble, following the cumulant expansion method of Pointin and Lundgren [Phys. Fluids **19**, 1459 (1976)]. The equation for vorticity fluctuations, obtained when a thermodynamic scaling limit is taken, is solved explicitly. The solution depends on an infinite sequence of negative "domain inverse temperatures," determined by the domain shape, which are obtained from solutions of a "vorticity mode" eigenvalue problem. An explicit expression for the thermodynamic curve relating inverse temperature and energy is found and is shown to depend on the geometry and not on the scale of the domain. Explicit formulas are then obtained for the time variance of the projection of the vorticity field onto each vorticity mode. The results are verified by two methods. First, for a chosen single-parameter family of domains, direct sampling of the microcanonical ensemble is used to demonstrate the accuracy of the formula for the thermodynamic curve. Second, direct numerical simulations are used to verify the formulas for the variance of the projections of the vorticity field, with convincing results.

DOI: 10.1103/PhysRevE.88.012109 PACS number(s): 05.20.Jj, 47.10.−g, 47.15.ki, 47.27.eb

## I. INTRODUCTION

Point-vortex models (e.g., Newton [1]) are widely held to be important and instructive, if somewhat idealized, paradigms relevant to the study of two-dimensional fluid turbulence [2–4], plasma physics [5], the dynamics of superfluids [6], and the statistical mechanics of long-range interacting particles [7,8]. There is also an interesting analogy between the statistical mechanics of the point-vortex system and models of self-gravitating particles used to investigate the self-organization of stellar systems [8].

A typical formulation is that of a neutral point-vortex gas, consisting of $N$ two-dimensional point vortices, equal numbers of which have circulation $\Gamma_i = \pm 1/N$ $(i = 1,\dots,N)$. The time evolution of vortex positions $\boldsymbol{x}_i = (x_i \;\; y_i)^T$, within a simply connected domain $\mathcal{D} \subset \mathbb{R}^2$, is governed by Hamilton's equations

$$\Gamma_i \dot{x}_i = -\frac{\partial H}{\partial y_i}, \quad \Gamma_i \dot{y}_i = \frac{\partial H}{\partial x_i}, \quad i = 1,\dots,N. \tag{1}$$

The Hamiltonian, which is a conserved quantity of the motion, is [9]

$$H(\boldsymbol{x}_1,\dots,\boldsymbol{x}_N) = -\sum_{i=j+1}^{N}\sum_{j=1}^{N}\Gamma_i\Gamma_j G(\boldsymbol{x}_i,\boldsymbol{x}_j) - \frac{1}{2}\sum_{i=1}^{N}\Gamma_i^2 g(\boldsymbol{x}_i,\boldsymbol{x}_i), \tag{2}$$

where $G(\boldsymbol{x},\boldsymbol{x}')$ is the Green's function of the first kind of the Laplacian in $\mathcal{D}$, i.e., satisfying the Dirichlet boundary condition

$$G(\boldsymbol{x},\boldsymbol{x}') = 0, \quad \text{for} \quad \boldsymbol{x} \text{ on } \partial\mathcal{D},$$

where $\partial\mathcal{D}$ is the boundary of $\mathcal{D}$. The function $g(\boldsymbol{x},\boldsymbol{x}')$ is given by

$$g(\boldsymbol{x},\boldsymbol{x}') = G(\boldsymbol{x},\boldsymbol{x}') - \frac{1}{2\pi}\log|\boldsymbol{x}-\boldsymbol{x}'|.$$

Note that it is the diagonal evaluation $g(\boldsymbol{x},\boldsymbol{x})$, sometimes known as the Robin function, that appears in (2).

The system is isolated and, consequently, subject to a suitable ergodic hypothesis, the statistics at a prescribed energy level $(H = E)$ are governed by the microcanonical ensemble

$$p(\boldsymbol{x}_1,\dots,\boldsymbol{x}_N) = \frac{\delta(E - H(\boldsymbol{x}_1,\dots,\boldsymbol{x}_N))}{W(E)}, \tag{3}$$

where $W(E)$ is the density of states (akin to a microcanonical partition function),

$$W(E) = \int_{\mathcal{D}^N} \delta(E - H(\boldsymbol{x}_1,\dots,\boldsymbol{x}_N))d\boldsymbol{x}_1\dots d\boldsymbol{x}_N. \tag{4}$$

Two quantities of particular interest are the (nondimensional) entropy $S$ and the inverse thermodynamic temperature $\beta$ given by

$$S(E) = \log W(E), \quad \beta(E) = \frac{1}{N}\frac{dS}{dE} = \frac{1}{N}\frac{W'(E)}{W(E)}. \tag{5}$$

In the present work a new solution, describing the limiting form as $N \to \infty$ of the entropy and inverse thermodynamic temperature curves, is derived. The new solution describes the statistics of the neutral point-vortex gas at energies (positive or negative) sufficiently low for a significant mean flow to be absent.

It is in fact straightforward to make numerical estimates of the density of states $W(E)$ using statistical sampling of the uniform distribution, i.e., by repeatedly generating random distributions of vortices in $\mathcal{D}$, calculating their energy, and constructing a histogram representation of the results [10,11]. Campbell and O'Neil [10] used results from the theory of $U$-statistics to show that, for certain $\mathcal{D}$ (e.g., a regular parallelogram), the density of states function converges

---

[*] gavin@math.ucl.ac.uk

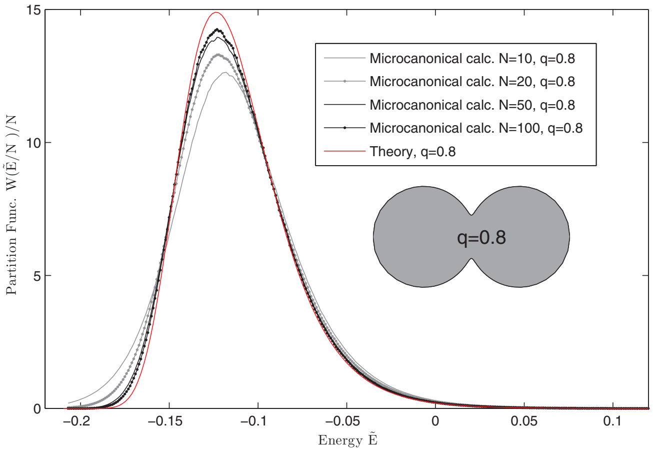

FIG. 1. (Color online) Convergence of statistical estimates of the density of states $W(\tilde{E}/N)/N \to W_t(\tilde{E})$ as $N \to \infty$. The calculations are for $N = 10$, 20, 50, and 100 vortices, respectively ($N/2$ positive and $N/2$ negative) for the Neumann oval shape illustrated (discussed in more detail in Sec. IV A). The statistical estimates of $W(E)$ are generated using the kernel density method described in Sec. IV B. The theoretical (red or upper) curve is the result obtained by numerical quadrature of Eq. (41).

according to

$$\lim_{N\to\infty} \frac{1}{N} W(\tilde{E}/N) = W_t(\tilde{E}). \tag{6}$$

That similar limiting behavior also holds in a general domain $\mathcal{D}$ appears likely. As a simple illustration [12], for the "Neumann oval" shape illustrated, Fig. 1 shows histogram-based estimates of $W(\tilde{E}/N)/N$ against $\tilde{E}$. Ignoring for the present the theoretical (red or upper) curve, convergence to the invariant function $W_t(\tilde{E})$, referred to here as the *thermodynamic density of states*, is arguably evident. It is to be emphasized that $W_t(\tilde{E})$ is a function of the scaled thermodynamic energy $\tilde{E} = NE$.

Evidently, if the limiting form of $W_t(\tilde{E})$, and the corresponding thermodynamic inverse temperature

$$\beta_t(\tilde{E}) = \frac{W_t'(\tilde{E})}{W_t(\tilde{E})} \tag{7}$$

are to be determined by the methods of statistical mechanics, the system (1) must be examined in the joint limit $N \to \infty$, $\tilde{E} = NE$ (constant), referred to hereafter as the *thermodynamic scaling limit*. This thermodynamic scaling limit, however, is not the standard textbook thermodynamic limit in which the domain area $|\mathcal{D}|$ is simultaneously increased (holding the vortex density $N/|\mathcal{D}|$ constant), and which might be expected to lead to a domain-independent equation of state for the system. The textbook limit has been studied mathematically by Fröhlich and Ruelle [13] and statistically by Campbell and O'Neil [10]. However, examination of (1) and (2), together with the appropriate logarithmic Green's functions defined in Appendix B, reveals that, under a rescaling of the domain with scale factor $\alpha$, the governing equations of the point-vortex system are invariant up to a change in the conserved energy $H \to H - (1/4\pi N)\log\alpha$. Consequently, no additional physics is uncovered by including rescaling of the domain size in the thermodynamic scaling limit, and relevant physics can in fact be obscured by the shift in energy [14]. It follows that, because of the long-range nature of the interactions in the vortex gas, the influence of the domain boundary is an inescapable feature of the system even as $N \to \infty$.

The thermodynamic scaling limit is to be contrasted with the *hydrodynamic* (or Euler) limit for which $E$ is held fixed as $N \to \infty$. The hydrodynamic limit leads to the well-known sinh-Poisson equation, satisfied by the streamfunction $\psi$ of the (leading-order) mean-flow,

$$\nabla^2\psi = C\sinh(\beta\psi) \tag{8}$$

(here $C$ is a constant determined by the integral constraint on the vorticity). Equation (8) can be obtained from either a variational principle based on a mean-field approximation [5] or by using the cumulant expansion method outlined in Sec. II A below [15]. In combination with the energy constraint, solutions of the sinh-Poisson equation in $\mathcal{D}$, subject to suitable boundary conditions, can be used to obtain a limiting thermodynamic relationship $\beta = \beta_h(E)$. However, $\beta_h(E)$ clearly cannot account for the limiting form $\beta_t(\tilde{E})$ discussed above. Not only does the energy scale differently with $N$, but it is also known [16] that $\beta_h(E)$ has a negative upper bound. By contrast, by inspection of Fig. 1, it is clear that $\beta_t(\tilde{E})$ takes both positive and negative values.

The thermodynamic scaling regime adopted here has been studied previously by Pointin and Lundgren [15] (PL76 hereafter) using the cumulant expansion method described in Sec. II A below. Under the assumption that a mean flow is absent, PL76 derived an equation [their Eq. (35)] describing the statistics of vorticity fluctuations. Here, it will be demonstrated that a variant of PL76's equation, the *vorticity fluctuation equation* [Eq. (32) below], together with appropriate boundary conditions, completely determines the statistics of the thermodynamic scaling regime. The main purpose of the present work is to present a solution to the vorticity fluctuation equation and to show that the new solution accounts for the shape of the thermodynamic density of states $W_t(\tilde{E})$ and therefore that of the corresponding thermodynamic caloric or inverse temperature curve $\beta_t(\tilde{E})$.

Section II presents a new treatment of PL76's cumulant equations in the thermodynamic scaling limit, resulting in the derivation of the vorticity fluctuation equation (32). PL76's method is adapted to emphasize the different roles played by vorticity and vortex density in the dynamics. In Sec. III the vorticity fluctuation equation is solved and explicit formulas are given for $W_t(\tilde{E})$ and $\beta_t(\tilde{E})$. The new solution leads to predictions of the amplitudes of fluctuations of the vorticity field, as measured by the projection of the vorticity field onto certain normal modes of the domain, to be defined. In Sec. IV the predictions of the new solution are tested, first by comparison with statistical reconstructions of $\beta_t(\tilde{E})$ and second by comparing the predicted variance of certain spatial projections of the vorticity field with the results of direct numerical simulations. In Sec. V conclusions are drawn.

## II. DERIVATION OF THE VORTICITY FLUCTUATION EQUATION

### A. The cumulant expansion

Here, PL76's derivation of the cumulant expansion for the neutral vortex gas is revisited from a new perspective. PL76 [15] obtained a hierarchy of cumulant equations satisfied by the marginal densities of (3), that is,

$$\begin{aligned} p_+(\boldsymbol{x}_1) &= \int_{\mathcal{D}^{N-1}} p(\boldsymbol{x}_1,\ldots,\boldsymbol{x}_N)d\boldsymbol{x}_2\cdots d\boldsymbol{x}_N, \\ p_-(\boldsymbol{x}_N) &= \int_{\mathcal{D}^{N-1}} p(\boldsymbol{x}_1,\ldots,\boldsymbol{x}_N)d\boldsymbol{x}_1\cdots d\boldsymbol{x}_{N-1}, \\ p_{++}(\boldsymbol{x}_1,\boldsymbol{x}_2) &= \int_{\mathcal{D}^{N-2}} p(\boldsymbol{x}_1,\ldots,\boldsymbol{x}_N)d\boldsymbol{x}_3\cdots d\boldsymbol{x}_N, \\ &\ldots, \end{aligned} \tag{9}$$

where the ± subscripts refer to vortices with positive (first $N/2$) and negative (remaining $N/2$) circulations respectively. An alternative starting point is to consider the vorticity and vortex density distributions

$$\omega(\boldsymbol{x}) = \sum_{i=1}^{N}\Gamma_i\delta(\boldsymbol{x}-\boldsymbol{x}_i), \quad \rho(\boldsymbol{x}) = \frac{1}{N}\sum_{i=1}^{N}\delta(\boldsymbol{x}-\boldsymbol{x}_i) \tag{10}$$

(where recall that here $\Gamma_i = \pm 1/N$). By denoting the ensemble average of a function $f(\boldsymbol{x}_1,\ldots,\boldsymbol{x}_N)$ by

$$\langle f\rangle = \int_{\mathcal{D}^N} f(\boldsymbol{x}_1,\ldots,\boldsymbol{x}_N)p(\boldsymbol{x}_1,\ldots,\boldsymbol{x}_N)d\boldsymbol{x}_1\ldots d\boldsymbol{x}_N, \tag{11}$$

the cumulant expansion can be developed in terms of the ensemble means

$$\begin{aligned} \omega_1(\boldsymbol{x}) &= \langle\omega(\boldsymbol{x})\rangle = \tfrac{1}{2}[p_+(\boldsymbol{x}) - p_-(\boldsymbol{x})], \\ \rho_1(\boldsymbol{x}) &= \langle\rho(\boldsymbol{x})\rangle = \tfrac{1}{2}[p_+(\boldsymbol{x}) + p_-(\boldsymbol{x})] \end{aligned} \tag{12}$$

and the *desingularized* second-order cumulants

$$\begin{aligned} \omega_2(\boldsymbol{x},\boldsymbol{x}') &= \langle[\omega(\boldsymbol{x})-\omega_1(\boldsymbol{x})][\omega(\boldsymbol{x}')-\omega_1(\boldsymbol{x}')]\rangle \\ &\quad -(1/N)\rho_1(\boldsymbol{x})\delta(\boldsymbol{x}-\boldsymbol{x}'), \\ c_2(\boldsymbol{x},\boldsymbol{x}') &= \langle[\rho(\boldsymbol{x})-\rho_1(\boldsymbol{x})][\omega(\boldsymbol{x}')-\omega_1(\boldsymbol{x}')]\rangle \\ &\quad -(1/N)\omega_1(\boldsymbol{x})\delta(\boldsymbol{x}-\boldsymbol{x}'), \\ \rho_2(\boldsymbol{x},\boldsymbol{x}') &= \langle[\rho(\boldsymbol{x})-\rho_1(\boldsymbol{x})][\rho(\boldsymbol{x}')-\rho_1(\boldsymbol{x}')]\rangle \\ &\quad -(1/N)\rho_1(\boldsymbol{x})\delta(\boldsymbol{x}-\boldsymbol{x}'). \end{aligned} \tag{13}$$

The unorthodox delta-function terms in (13) are "natural" in the sense that they remove all singular terms and permit $\omega_2$, $c_2$, and $\rho_2$ to be expressed in terms of $p_{++}$, $p_{+-}$, etc. It is straightforward to define higher cumulants by analogy. Some relevant expressions are given in Appendix A.

The advantage of recasting PL76's cumulant expansion in this fashion are twofold. First, it simplifies some of PL76's expressions, notably the energy equation [Eq. (16) below]. Second, it emphasizes that vorticity and vortex density scale differently in the hydrodynamic and thermodynamic limits introduced above, with the more fundamental terms, in the sense that they eventually determine the thermodynamic curve, being those related to vorticity and its fluctuations, $\omega_1$ and $\omega_2$, respectively. It is useful at this point to introduce a streamfunction $\psi_1$ for the mean flow arising from the mean vorticity distribution $\omega_1$, satisfying

$$\begin{aligned} &\psi_1(\boldsymbol{x}) = \int_{\mathcal{D}} G(\boldsymbol{x},\boldsymbol{x}')\omega_1(\boldsymbol{x}')d\boldsymbol{x}' \quad \text{or} \\ &\nabla^2\psi_1 = \omega_1, \quad \psi_1 = 0 \quad \text{on } \partial\mathcal{D}. \end{aligned}$$

Here, and throughout the rest of this work unless otherwise indicated, the Laplacian and gradient operator act on the variable $\boldsymbol{x}$. Similarly, one can introduce streamfunctions for the higher order cumulants, e.g.,

$$\begin{aligned} \psi_2(\boldsymbol{x},\boldsymbol{x}') &= \int_{\mathcal{D}} G(\boldsymbol{x},\boldsymbol{x}'')\omega_2(\boldsymbol{x}'',\boldsymbol{x}')d\boldsymbol{x}'' \\ &= \langle[\psi(\boldsymbol{x})-\psi_1(\boldsymbol{x})][\omega(\boldsymbol{x}')-\omega_1(\boldsymbol{x}')]\rangle \\ &\quad -\frac{1}{N}\rho_1(\boldsymbol{x}')G(\boldsymbol{x},\boldsymbol{x}'). \end{aligned} \tag{14}$$

In order to express the energy in terms of the cumulants defined above, it suffices to take the ensemble average of $H$,

$$\langle H\rangle = \int_{\mathcal{D}^N} H(\boldsymbol{x}_1,\ldots,\boldsymbol{x}_N)p(\boldsymbol{x}_1,\ldots,\boldsymbol{x}_N)d\boldsymbol{x}_1\cdots dx_1\boldsymbol{x}_N = E. \tag{15}$$

Substituting for $H$ from its definition (2) and for the cumulants defined above leads to

$$\begin{aligned} E &= -\frac{1}{2}\int_{\mathcal{D}^2} G(\boldsymbol{x},\boldsymbol{x}')[\omega_1(\boldsymbol{x})\omega_1(\boldsymbol{x}')+\omega_2(\boldsymbol{x},\boldsymbol{x}')]d\boldsymbol{x}\,d\boldsymbol{x}' \\ &\quad -\frac{1}{2N}\int_{\mathcal{D}} g(\boldsymbol{x},\boldsymbol{x})\rho_1(\boldsymbol{x})d\boldsymbol{x}. \end{aligned} \tag{16}$$

Equation (16), which is exact, simplifies PL76's equivalent expression [their Eq. (12)], and more importantly it admits simple interpretation. The first term involving $\omega_1$ is the energy of the (ensemble) mean flow, exactly as appears in regular Eulerian two-dimensional fluid dynamics. The second term involving $\omega_2$ gives the energy associated with fluctuations or eddies about this mean flow, and the final density correction term corrects for the de-singularizing term in the definition (13) of $\omega_2$.

PL76's cumulant equations follow from applying the gradient operator to the marginal densities. For example, using $\nabla_1$ to denote the gradient operation with respect to variable $\boldsymbol{x}_1$, one has

$$\begin{aligned} \nabla_1 p_+(\boldsymbol{x}_1) &= \frac{1}{W(E)}\int_{\mathcal{D}^{N-1}} \nabla_1\delta(H-E)d\boldsymbol{x}_2\cdots d\boldsymbol{x}_N \\ &= -\frac{1}{W(E)}\int_{\mathcal{D}^{N-1}} \nabla_1 H\,\partial_E\,\delta(H-E)d\boldsymbol{x}_2\cdots d\boldsymbol{x}_N \\ &= -N(\partial_{\tilde{E}}+\beta)\int_{\mathcal{D}^{N-1}} \nabla_1 H(\boldsymbol{x}_1,..,\boldsymbol{x}_N) \\ &\quad \times p(\boldsymbol{x}_1,..,\boldsymbol{x}_N)d\boldsymbol{x}_2\cdots d\boldsymbol{x}_N, \end{aligned}$$

where $\tilde{E} = NE$ has been substituted and use has been made of the identity

$$\partial_E p = W^{-1}\partial_E\delta(E-H) - \beta N p, \tag{17}$$

obtained from differentiating (3). Expanding $H$ in terms of its definition (2), and then substituting $\boldsymbol{x}$ for $\boldsymbol{x}_1$ and $\boldsymbol{x}'$ for the variable of integration, which cannot be evaluated in each term in the sum, leads to

$$\nabla p_+(\boldsymbol{x}) = (\partial_{\tilde{E}} + \beta)\left(\frac{1}{2}\int_{\mathcal{D}} \nabla G(\boldsymbol{x},\boldsymbol{x}')[p_{++}(\boldsymbol{x},\boldsymbol{x}') - p_{+-}(\boldsymbol{x},\boldsymbol{x}')]d\boldsymbol{x}' - \frac{1}{N}\int_{\mathcal{D}} \nabla G(\boldsymbol{x},\boldsymbol{x}')p_{++}(\boldsymbol{x},\boldsymbol{x}')d\boldsymbol{x}' + \frac{1}{2N}\nabla g(\boldsymbol{x},\boldsymbol{x})p_+(\boldsymbol{x})\right). \tag{18}$$

A similar expression for $\nabla p_-$ is given in Appendix A [Eq. (A1)]. By combining (18) and (A1), analogous expressions for $\nabla\omega_1$ and $\nabla\rho_1$ are found to be

$$\nabla\omega_1(\boldsymbol{x}) = (\partial_{\tilde{E}} + \beta)\left(\rho_1(\boldsymbol{x})\nabla\psi_1(\boldsymbol{x}) + \int_{\mathcal{D}} \nabla G(\boldsymbol{x},\boldsymbol{x}')c_2(\boldsymbol{x},\boldsymbol{x}')d\boldsymbol{x}' + \frac{1}{2N}\omega_1(\boldsymbol{x})\nabla g(\boldsymbol{x},\boldsymbol{x})\right), \tag{19}$$

$$\nabla\rho_1(\boldsymbol{x}) = (\partial_{\tilde{E}} + \beta)\left(\omega_1(\boldsymbol{x})\nabla\psi_1(\boldsymbol{x}) + \int_{\mathcal{D}} \nabla G(\boldsymbol{x},\boldsymbol{x}')\omega_2(\boldsymbol{x},\boldsymbol{x}')d\boldsymbol{x}' + \frac{1}{2N}\rho_1(\boldsymbol{x})\nabla g(\boldsymbol{x},\boldsymbol{x})\right). \tag{20}$$

Equivalent equations for second-order and higher order cumulants are obtained by following the same procedure. Details are given in Appendix A. The resulting second-order cumulant equations are

$$\begin{aligned}\nabla\omega_2(\boldsymbol{x},\boldsymbol{x}') = {}& (\partial_{\tilde{E}} + \beta)\Bigg(\rho_1(\boldsymbol{x})\nabla\psi_2(\boldsymbol{x},\boldsymbol{x}') + c_2(\boldsymbol{x},\boldsymbol{x}')\nabla\psi_1(\boldsymbol{x}) + \int_{\mathcal{D}} \nabla G(\boldsymbol{x},\boldsymbol{x}'')c_3(\boldsymbol{x},\boldsymbol{x}',\boldsymbol{x}'')d\boldsymbol{x}''\\ &+ \frac{1}{N}\nabla G(\boldsymbol{x},\boldsymbol{x}')[\rho_2(\boldsymbol{x},\boldsymbol{x}') + \rho_1(\boldsymbol{x})\rho_1(\boldsymbol{x}')] + \frac{1}{2N}\omega_2(\boldsymbol{x},\boldsymbol{x}')\nabla g(\boldsymbol{x},\boldsymbol{x})\Bigg)\\ &+ (\partial_{\tilde{E}}\omega_1(\boldsymbol{x}'))\left(\rho_1(\boldsymbol{x})\nabla\psi_1(\boldsymbol{x}) + \int_{\mathcal{D}} \nabla G(\boldsymbol{x},\boldsymbol{x}'')c_2(\boldsymbol{x},\boldsymbol{x}'')d\boldsymbol{x}'' + \frac{1}{2N}\omega_1(\boldsymbol{x})\nabla g(\boldsymbol{x},\boldsymbol{x})\right),\end{aligned} \tag{21}$$

$$\begin{aligned}\nabla c_2(\boldsymbol{x},\boldsymbol{x}') = {}& (\partial_{\tilde{E}} + \beta)\Bigg(\omega_1(\boldsymbol{x})\nabla\psi_2(\boldsymbol{x},\boldsymbol{x}') + \omega_2(\boldsymbol{x},\boldsymbol{x}')\nabla\psi_1(\boldsymbol{x}) + \int_{\mathcal{D}} \nabla G(\boldsymbol{x},\boldsymbol{x}'')\omega_3(\boldsymbol{x},\boldsymbol{x}',\boldsymbol{x}'')d\boldsymbol{x}''\\ &+ \frac{1}{N}\nabla G(\boldsymbol{x},\boldsymbol{x}')[c_2(\boldsymbol{x}',\boldsymbol{x}) + \omega_1(\boldsymbol{x})\rho_1(\boldsymbol{x}')] + \frac{1}{2N}c_2(\boldsymbol{x},\boldsymbol{x}')\nabla g(\boldsymbol{x},\boldsymbol{x})\Bigg)\\ &+ (\partial_{\tilde{E}}\omega_1(\boldsymbol{x}'))\left(\omega_1(\boldsymbol{x})\nabla\psi_1(\boldsymbol{x}) + \int_{\mathcal{D}} \nabla G(\boldsymbol{x},\boldsymbol{x}'')\omega_2(\boldsymbol{x},\boldsymbol{x}'')d\boldsymbol{x}'' + \frac{1}{2N}\rho_1(\boldsymbol{x})\nabla g(\boldsymbol{x},\boldsymbol{x})\right),\end{aligned} \tag{22}$$

$$\begin{aligned}\nabla\rho_2(\boldsymbol{x},\boldsymbol{x}') = {}& (\partial_{\tilde{E}} + \beta)\Bigg(\omega_1(\boldsymbol{x})\nabla\phi_2(\boldsymbol{x}',\boldsymbol{x}) + c_2(\boldsymbol{x},\boldsymbol{x}')\nabla\psi_1(\boldsymbol{x}) + \int_{\mathcal{D}} \nabla G(\boldsymbol{x},\boldsymbol{x}'')c_3(\boldsymbol{x}',\boldsymbol{x},\boldsymbol{x}'')d\boldsymbol{x}''\\ &+ \frac{1}{N}\nabla G(\boldsymbol{x},\boldsymbol{x}')[\omega_2(\boldsymbol{x},\boldsymbol{x}') + \omega_1(\boldsymbol{x})\omega_1(\boldsymbol{x}')] + \frac{1}{2N}\rho_2(\boldsymbol{x},\boldsymbol{x}')\nabla g(\boldsymbol{x},\boldsymbol{x})\Bigg)\\ &+ (\partial_{\tilde{E}}\omega_1(\boldsymbol{x}'))\left(\omega_1(\boldsymbol{x})\nabla\psi_1(\boldsymbol{x}) + \int_{\mathcal{D}} \nabla G(\boldsymbol{x},\boldsymbol{x}'')\omega_2(\boldsymbol{x},\boldsymbol{x}'')d\boldsymbol{x}'' + \frac{1}{2N}\rho_1(\boldsymbol{x})\nabla g(\boldsymbol{x},\boldsymbol{x})\right).\end{aligned} \tag{23}$$

The second-order cumulant expression $\phi_2$ and the desingularized third-order cumulants $\omega_3$ and $c_3$ are defined in Appendix A,

Together, the energy equation (16), the ensemble mean equations (19) and (20), the fluctuation equations (21)–(23), and the analogous equations for higher order cumulants [cf. PL76's Eq. (17)] form an infinite hierarchy that, in principle, exactly describes the statistics of the point-vortex system for an arbitrary number of vortices $N$. Progress can evidently be made by consideration of the limit $N \to \infty$. PL76 realized that the cumulant hierarchy can serve as the parent model for more than one possible asymptotic limit. In particular, the hydrodynamic and thermodynamic regimes can be explored separately by fixing $E$ to be a constant as $N \to \infty$ (hydrodynamic), or fixing $\tilde{E} = NE$ as $N \to \infty$ (thermodynamic). It is worth noting that other limits, as yet unexplored, might also lead to nontrivial results.

### B. The vorticity fluctuation equation

In order to obtain the governing equation of the thermodynamic scaling regime, the thermodynamic limit [$N \to \infty$, $\tilde{E} = NE$ (constant)] must be taken. When taking this limit, PL76 simultaneously truncate the infinite hierarchy of cumulant equations. No formal justification of this truncation is given, beyond citing the success of a similar approach for other problems in physics.

The following conjecture would, if proved, provide formal justification for PL76's truncation. The conjecture is based on the scaling and convergence properties of the ensemble-averaged quantities defined above, identified in the statistical sampling calculations described below, as the number of vortices $N$ is varied. It will be termed the "asymptotic hierarchy conjecture" and, simply stated, is that the cumulant equations admit asymptotic solutions in the small parameter $\epsilon = N^{-1/2}$.

Here, the existence of an asymptotic hierarchy satisfying the cumulant equations in the thermodynamic limit will be assumed. However, if preferred by the reader, this assumption can be replaced by truncating the cumulant equations following PL76, the results of the two procedures being essentially equivalent. The relevant asymptotic hierarchy in the thermodynamic scaling limit relies upon the assumption of no mean flow ($\omega_1 = 0$). Symmetry of the microcanonical ensemble then dictates that odd vorticity moments are zero (e.g., $\omega_3 = 0$) and consequently cross-correlations involving odd powers of the vorticity are also zero [e.g., $c_2 = 0$; see Eq. (22)]. It is natural then to look for asymptotic series solutions for the remaining terms of the form

$$\begin{aligned} \rho_1(\boldsymbol{x}) &= \rho_0 + \epsilon^2 \rho_1^{(1)} + \cdots, \\ \omega_2(\boldsymbol{x},\boldsymbol{x}') &= \epsilon^2\big(\omega_2^{(0)} + \epsilon^2 \omega_2^{(1)} + \cdots\big), \\ \rho_2(\boldsymbol{x},\boldsymbol{x}') &= \epsilon^4\big(\rho_2^{(0)} + \epsilon^2 \rho_2^{(1)} + \dots\big), \quad \text{etc.} \end{aligned} \tag{24}$$

Here$\rho_0 = |\mathcal{D}|^{-1}$, the inverse of the domain area, is the leading term in the vortex density expansion in the low-energy thermodynamic scaling regime. Note that an exactly uniform distribution of vortices corresponds to $\rho_1(\boldsymbol{x}) = \rho_0$.

Inserting the expansions (24) into (21) and equating at the leading power of $\epsilon^2$ leads to the following equation satisfied by the leading-order vorticity fluctuations:

$$\nabla\omega_2^{(0)}(\boldsymbol{x},\boldsymbol{x}') = \rho_0(\partial_{\tilde{E}} + \beta)\big(\nabla\psi_2^{(0)}(\boldsymbol{x},\boldsymbol{x}') + \rho_0\nabla G(\boldsymbol{x},\boldsymbol{x}')\big), \tag{25}$$

where $\omega_2^{(0)}$ is symmetric in its arguments and is subject to an integral constraint

$$\int_{\mathcal{D}} \omega_2^{(0)}(\boldsymbol{x},\boldsymbol{x}')d\boldsymbol{x} = -\rho_0 \tag{26}$$

obtained by inserting the expansion (24) into the definition (13). Similarly, the leading order correction to the mean vortex density is found to be given by

$$\begin{aligned} \nabla\rho_1^{(1)}(\boldsymbol{x}) = (\partial_{\tilde{E}} + \beta)\int_{\mathcal{D}} \nabla G(\boldsymbol{x},\boldsymbol{x}')\omega_2^{(0)}(\boldsymbol{x},\boldsymbol{x}')d\boldsymbol{x}' \\ + \frac{1}{2}\beta\rho_0\nabla g(\boldsymbol{x},\boldsymbol{x}). \end{aligned} \tag{27}$$

The energy equation (16) is at leading order given by

$$\begin{aligned} \tilde{E} &= -\frac{1}{2}\int_{\mathcal{D}} \psi_2^{(0)}(\boldsymbol{x},\boldsymbol{x})d\boldsymbol{x} - \frac{g_0}{2}, \\ \text{where} \quad g_0 &= \rho_0\int_{\mathcal{D}} g(\boldsymbol{x},\boldsymbol{x})d\boldsymbol{x}. \end{aligned} \tag{28}$$

Upon taking the divergence of (25), the resulting equation, together with (27) and (28), can be seen to be related to equations appearing in PL76 [15]. [Specifically, the divergence of Eq. (25) and Eq. (28) are identical to Eqs. (35) and (37) of PL76, upon identifying $\omega_2^{(0)}$ with PL76's $F(1,2) - 1$, and rescaling $\beta \to 8\pi\beta$, and (27) is analogous to PL76's Eq. (36).]

PL76 used equation (25) both to obtain an exact solution in the special situation of a doubly-periodic domain and to derive an equation for the thermodynamic curve in the limit $\beta \to \infty$, corresponding to large negative energies. Taking the divergence of (25) results in

$$\nabla^2\omega_2^{(0)} = \rho_0(\partial_{\tilde{E}} + \beta)\omega_2^{(0)} + \beta\rho_0\delta(\boldsymbol{x} - \boldsymbol{x}'). \tag{29}$$

In the doubly-periodic domain, the issue of boundary conditions does not arise, and the periodic basis of sinusoidal modes allows the integral constraint (26) to be satisfied automatically. PL76 consequently were able to use (29) directly to obtain a solution [their Eq. (41)] that can be regarded as a particular case of the general solution given below. In fact, their solution had been previously found using the random-phase approximation by Edwards and Taylor [17]. In the limit $\beta \to \infty$, PL76 argue that $|\partial_{\tilde{E}}| \ll \beta$ and that correlations become short range so that boundary conditions can be replaced with decay conditions at large radius. Equation (29) then has a solution involving the modified Bessel function $K_0(\cdot)$,

$$\omega_2^{(0)}(\boldsymbol{x},\boldsymbol{x}') = -\frac{\beta\rho_0^2}{2\pi}K_0((\beta\rho_0)^{1/2}|\boldsymbol{x} - \boldsymbol{x}'|). \tag{30}$$

Equation (30) satisfies the integral constraint (26), and, after insertion in (28) and careful expansion of the resulting integral, leads to the thermodynamic relation

$$\beta(\tilde{E}) = \frac{1}{\rho_0}\exp\left(-8\pi\tilde{E} + 2\log 2 - 2\gamma\right), \tag{31}$$

where $\gamma \approx 0.57722$ is the Euler gamma constant. Edwards and Taylor [17] had also previously obtained (31), starting from the random-phase approximation. The $\tilde{E} \to -\infty$ asymptotic result (31) provides a useful check on the exact solution to be obtained below.

To obtain a general solution to the system (25)–(28) it turns out to be necessary to integrate (25) rather than take its divergence as above. By using the integral constraint (26) to obtain the arbitrary function of integration, (25) can be expressed as an integro-differential equation for $\omega_2^{(0)}$:

$$\omega_2^{(0)} = -\rho_0^2 + \rho_0(\partial_{\tilde{E}} + \beta)\mathcal{L}\omega_2^{(0)} + \beta\rho_0^2\mathcal{L}\delta(\boldsymbol{x} - \boldsymbol{x}'), \tag{32}$$

where the linear integral operator $\mathcal{L}$ acts on a function $\phi(\boldsymbol{x})$ according to

$$\begin{aligned} \mathcal{L}\phi(\boldsymbol{x}) &\equiv \int_{\mathcal{D}} K(\boldsymbol{x},\bar{\boldsymbol{x}})\,\phi(\bar{\boldsymbol{x}})\,d\bar{\boldsymbol{x}}, \\ \text{where} \quad K(\boldsymbol{x},\bar{\boldsymbol{x}}) &= G(\boldsymbol{x},\bar{\boldsymbol{x}}) - G_0(\boldsymbol{x}) - G_0(\bar{\boldsymbol{x}}), \\ G_0(\boldsymbol{x}) &= \rho_0\int_{\mathcal{D}} G(\boldsymbol{x},\bar{\boldsymbol{x}})d\bar{\boldsymbol{x}}. \end{aligned} \tag{33}$$

Equation (32) is the key equation of the thermodynamic scaling regime, analogous to the sinh-Poisson equation in the hydrodynamic regime. Henceforth (32) will be referred to as the *vorticity fluctuation equation* and its solution will be described next.

## III. SOLUTION OF THE VORTICITY FLUCTUATION EQUATION

The key to solving (32) is the identification of a natural basis for the vorticity fluctuation field $\omega_2^{(0)}$. It follows from the symmetry of the kernel $K(\boldsymbol{x},\bar{\boldsymbol{x}})$, and the close relationship between $K$ and the well-studied Dirichlet Laplacian kernel $G(\boldsymbol{x},\bar{\boldsymbol{x}})$, that the compact operator $\mathcal{L}$ is self-adjoint. The

Hilbert-Schmidt theorem [18] then states that the eigenvalue problem

$$\mathcal{L}\Phi = \frac{1}{\beta\rho_0}\Phi, \quad j = 0,1,2,\ldots \tag{34}$$

generates a set of real eigenvalues $\{\beta_j\}$ with corresponding eigenfunctions $\{\Phi_j(\boldsymbol{x})\}$ that form a complete orthonormal basis for square-integrable functions defined on $\mathcal{D}$. Importantly, $\Phi_0(\boldsymbol{x}) =$ constant is the first eigenfunction. It follows that the remaining eigenfunctions, referred to hereafter as the *vorticity modes*, satisfy

$$\int_{\mathcal{D}} \Phi_j(\boldsymbol{x})d\boldsymbol{x} = 0, \quad j = 1,2,3\ldots \tag{35}$$

by orthogonality. The corresponding eigenvalues $\{\beta_j\}$, for $j \geqslant 1$, will be referred to as the *domain inverse temperatures* (DITs hereafter). The DITs are all negative, and by construction they depend only on the geometry of the domain; i.e., they are invariant under a rescaling of the domain.

Evidently, it makes sense to seek solutions of (32) in the form of an expansion in the basis functions $\{\Phi_k\}$,

$$\omega_2^{(0)}(\boldsymbol{x},\boldsymbol{x}') = -\rho_0^2 + \rho_0 \sum_{j=1}^{\infty}\sum_{k=1}^{\infty} a_{jk}(\tilde{E})\Phi_j(\boldsymbol{x})\Phi_k(\boldsymbol{x}'). \tag{36}$$

The ansatz (36) automatically satisfies the integral constraint (26) because the first integral (35) of each vorticity mode vanishes. Inserting (36) into (32) and equating coefficients leads to

$$\beta_j a_{jk} = (\partial_{\tilde{E}} + \beta)a_{jk} + \beta\delta_{jk}(j,k \geqslant 1). \tag{37}$$

Solutions of the homogeneous equation for $a_{jk}$ are unphysical, i.e., unbounded as $\tilde{E} \to -\infty$; hence only the diagonal elements are nonzero. It follows that the solution is consistent with the $\boldsymbol{x} \leftrightarrow \boldsymbol{x}'$ symmetry implicit in the definition (13).

Evidently the inverse temperature $\beta$ in (37) must be regarded as a function of the scaled energy in the thermodynamic scaling limit, i.e., $\beta = \beta_t(\tilde{E})$ in (37). The diagonal terms in equation (37) can be obtained in terms of the corresponding entropy

$$S_t(\tilde{E}) = \int^{\tilde{E}} \beta_t(\hat{E})d\hat{E}$$

by direct integration:

$$a_{jj}(\tilde{E}) = -1 - \beta_j \exp\left(-[S_t(\tilde{E}) - \beta_j\tilde{E}]\right) \times \int_{-\infty}^{\tilde{E}} \exp\left(S_t(\hat{E}) - \beta_j\hat{E}\right)d\hat{E}. \tag{38}$$

Inserting (36) into the energy equation (28) results in

$$-\frac{1}{2}\sum_{j=1}^{\infty}\frac{a_{jj}}{\beta_j} = \tilde{E} - \tilde{E}_0, \quad \text{where} \quad \tilde{E}_0 = \frac{G_{00} - g_0}{2} \quad \text{and}$$

$$G_{00} = \rho_0^2 \int_{\mathcal{D}^2} G(\boldsymbol{x},\bar{\boldsymbol{x}})d\boldsymbol{x}\, d\bar{\boldsymbol{x}}. \tag{39}$$

Inserting (37) into the sum in (39), and substituting $W_t = \exp(S_t)$, results in the linear integral equation

$$(\tilde{E} - \tilde{E}_0)W_t(\tilde{E}) = \frac{1}{2}\sum_{j=1}^{\infty}\left(\frac{W_t(\tilde{E})}{\beta_j} + \int_{-\infty}^{\tilde{E}} W_t(\hat{E})\exp[\beta_j(\tilde{E} - \hat{E})]d\hat{E}\right). \tag{40}$$

Equation (40) can be solved by taking its Fourier transform. The result is

$$W_t(\tilde{E}) = \frac{W_0}{\sqrt{2\pi}}\int_{-\infty}^{\infty} f_1(k;\beta_j)\exp[i(\tilde{E} - \tilde{E}_0)k - i f_2(k;\beta_j)]dk, \tag{41}$$

where $f_1$ and $f_2$ are real-valued functions given by

$$f_1(k;\beta_j) = \prod_{j=1}^{\infty}\left(1 + \frac{k^2}{\beta_j^2}\right)^{-1/4}, \tag{42}$$

$$f_2(k;\beta_j) = \frac{1}{2}\sum_{j=1}^{\infty}\left[\frac{k}{\beta_j} - \tan^{-1}\left(\frac{k}{\beta_j}\right)\right], \tag{43}$$

and $W_0$ is a normalizing constant. The corresponding inverse temperature can be written, in a form convenient for numerical quadrature, as the ratio of the two real integrals:

$$\beta_t(\tilde{E}) = -\frac{\int_0^{\infty} k f_1(k;\beta_j)\sin[k(\tilde{E} - \tilde{E}_0) - f_2(k;\beta_j)]dk}{\int_0^{\infty} f_1(k;\beta_j)\cos[k(\tilde{E} - \tilde{E}_0) - f_2(k;\beta_j)]dk}. \tag{44}$$

It is evident from (44) that the limiting thermodynamic curve is completely determined, up to a shift in the ordinate due to a change [19] in $\tilde{E}_0$, by the distribution of DITs $\{\beta_j\}$. The amplitude function $f_1(k)$ decays exponentially as $k \to \infty$, rendering numerical quadrature of (44) straightforward. The domain-dependent constants $\tilde{E}_0$ are obtained by Clenshaw-Curtis quadrature [20] and the values obtained are $\tilde{E}_0 = -0.09979$ for the $q = 0.3$ oval and $\tilde{E}_0 = -0.1114$ for the $q = 0.8$ oval (four significant figures in each case).

Inserting the expression (41) for $W_t(\tilde{E})$ into (38), and evaluating the $\hat{E}$-integral results, allows the diagonal coefficients $a_{jj}$ to be evaluated:

$$a_{jj}(\tilde{E}) = -\frac{\int_0^{\infty} f_1(k)(k^2 + \beta_j^2)^{-1}\{k^2\cos[k(\tilde{E} - \tilde{E}_0) - f_2(k)] + \beta_j k\sin[k(\tilde{E} - \tilde{E}_0) - f_2(k)]\}dk}{\int_0^{\infty} f_1(k)\cos[k(\tilde{E} - \tilde{E}_0) - f_2(k)]dk}. \tag{45}$$

The coefficients $\{a_{jj}\}$ determine the partitioning of the energy into fluctuations associated with each vorticity mode. It will be shown below that they have a simple interpretation in terms of the variance of the projection of the vorticity field $\omega(\boldsymbol{x})$ onto the corresponding vorticity mode $\Phi_j(\boldsymbol{x})$. Changes in energy partitioning among the vorticity modes, as $\tilde{E}$ increases, will be seen to give insight into the nature of the transition between states without and with a mean flow.

## IV. VERIFICATION OF THE VORTICITY FLUCTUATION SOLUTION

### A. Determination of domain inverse temperatures

In order to compare the predictions of the formulas (44) and (45) with the results of the direct statistical and dynamical calculations described below, it is first necessary to find the DITs $\{\beta_j\}$ for the domain $\mathcal{D}$ under investigation. In general the DITs must be found numerically. One exception is for $\mathcal{D}$ a circle, for which all DITs can be expressed in terms of Bessel function zeros. However, the microcanonical ensemble (3) is not correct for the circle due to the additional constraint of conservation of angular momentum [21].

Evidently, the new formulas (44) and (45) should be tested for domains for which (3) is the correct ensemble. A convenient choice is a single-parameter $(0 \leqslant q < 1)$ family [22] of equal-area "Neumann ovals." As $q$ is varied the domain $\mathcal{D}$ changes smoothly between a circle $(q = 0)$ and two touching circles $(q = 1)$. Two intermediate cases are illustrated in Fig. 2, with (a) $q = 0.3$ and (b) $q = 0.8$. The Neumann ovals are conformal to the unit circle with map given by

$$z = \frac{\alpha(q)Z}{(1 - q^2Z^2)} \quad \text{with} \quad \alpha(q) = \frac{(1 - q^4)}{(1 + q^4)^{1/2}}, \tag{46}$$

where $z \in \mathbb{C}$ is identified with $\boldsymbol{x} \in \mathbb{R}^2$ in the Neumann oval domain, and $Z \in \mathbb{C}$ with the circle domain. The advantage of using a conformal map is that the Green's function $G(\boldsymbol{x},\boldsymbol{x}')$ appearing in the Hamiltonian (2) is easily found. The relevant formulas are given in Appendix B.

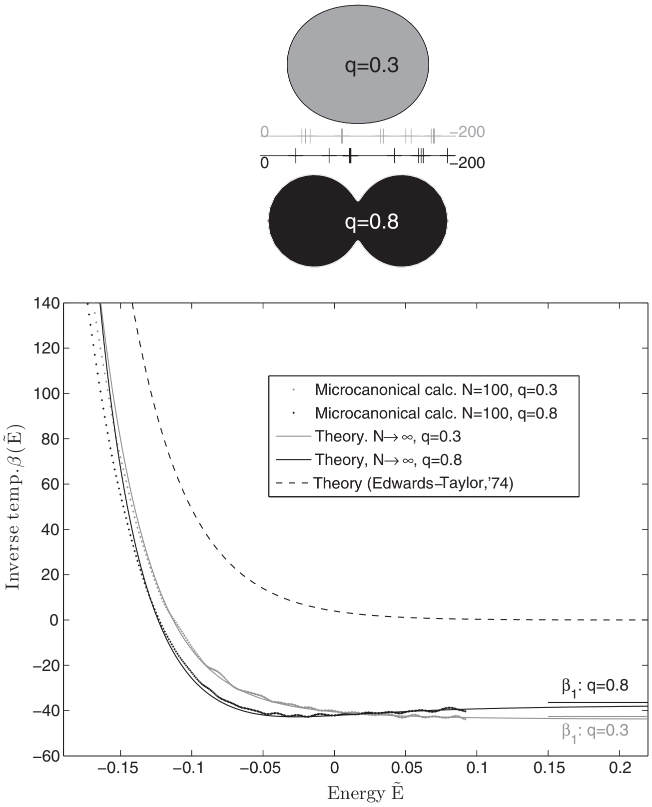

FIG. 2. (a) The $q = 0.3$ Neumann oval domain (top) and $q = 0.8$ (bottom) domain, and the distributions of DITs within the range $\beta_j \in [0, -200]$ for each. (b) The statistical estimates of $\beta(\tilde{E})$ (broken curves) versus theoretical predictions [solid curves, Eq. (44)]. Gray curves show results for the $q = 0.3$ Neumann oval domain and black curves the $q = 0.8$ domain. The dashed curve shows the Edwards-Taylor estimate (see text). The first DIT $(\beta_1)$ is also marked for the two domains.

There are numerous numerical methods that might be adapted to solve the eigenvalue problem (34) and obtain the DITs $\{\beta_j\}$. A convenient choice, which exploits the conformal map (46), is to adapt the Fourier-Chebyshev spectral method (e.g., Trefethen [20]). Details of how the spectral methods are adapted to solve (34) in a general conformal domain $\mathcal{D}$ are given in Appendix C.

The distributions of DITs within the range $0 > \beta_j > -200$, for the two domains illustrated, (a) $q = 0.3$, (b) $q = 0.8$, is shown in Fig. 2 (lines with ticks). The significant difference between the two domains is that the first three DITs for $q = 0.3$ are tightly clustered $(\beta_1 = -42.61,\ \beta_2 = -46.15$, and $\beta_3 = -51.02)$, whereas for $q = 0.8$ the first DIT is well separated from the subsequent ones $(\beta_1 = -36.37,\ \beta_2 = -70.15$, and $\beta_3 = -91.12)$. This qualitative difference between the two domains will be shown to be significant in determining the partitioning of energy among the vorticity modes.

### B. Verification by statistical sampling of the microcanonical ensemble

Statistical sampling of the uniform distribution [10,11] has previously been used to generate (unnormalized) histogram representations of the density of states $W(E)$. The results of both Campbell and O'Neil [10] and Fig. 1 suggest that convergence of $W(\tilde{E}/N)/N$ to an invariant function $W_t(\tilde{E})$ is evident for as few as $N = 100$ vortices. In Sec. III the theoretical form for $W_t(\tilde{E})$ was shown to be (41). Equation (41) has been evaluated by numerical quadrature (see below) and plotted on Fig. 1 (red or upper curve). Comparison with the finite-$N$ statistical results reveals that (41) is indeed a plausible limiting curve for the particular domain in question.

Our main focus here, however, will be on the more stringent test provided by convergence toward $\beta_t(\tilde{E}) = W_t'(\tilde{E})/W_t(\tilde{E})$, given by (44). The results of Fig. 1 suggest that numerical verification of (44) is computationally feasible using only $N = 100$ vortices. A robust verification of (44) requires comparison between domains with significantly different distributions of DITs $\{\beta_j\}$. Two suitable domains are the Neumann ovals with (a) $q = 0.3$ and (b) $q = 0.8$ introduced above.

To estimate $\beta_t(\tilde{E}) = W_t'(\tilde{E})/W_t(\tilde{E})$ for each domain, the uniform distribution is sampled by generating $10^7$ random locations within the ovals. Repeatedly, a random selection of $N = 100$ of these locations is made for the vortices ($N/2$ positive, $N/2$ negative), and each time a sampled energy $\tilde{E}_i = NH$ is calculated for the resulting distribution of vortices using (2). The distributions $W_t(\tilde{E})$ and $W_t'(\tilde{E})$ are then generated from $M = 10^7$–$10^8$ sampled values of $\tilde{E}_i$ using the kernel density estimation method [23], with Gaussian kernels. Specifically, for samples $\{\tilde{E}_i\}$ $(i = 1, \ldots, M)$, the estimates are

$$W_t(\tilde{E}) = \frac{1}{M}\sum_{i=1}^{M} K_d\left(\frac{\tilde{E} - \tilde{E}_i}{\sigma}\right), \tag{47}$$

$$W_t'(\tilde{E}) = -\frac{1}{\sigma M}\sum_{i=1}^{M} K_d'\left(\frac{\tilde{E} - \tilde{E}_i}{\sigma}\right), \tag{48}$$

where $K_d(x) = \exp(-x^2/2)$ is the Gaussian kernel. The kernel width $\sigma$ should be chosen to minimize the expected error due to bias ($\sigma$ large) and variance ($\sigma$ small). Although there is a large body of theory [23] describing how best to choose $\sigma$ to minimize errors in $W_t$, in the construction above, we are not aware of a corresponding theory to minimize error in $\beta_t$, the main quantity of interest here. In the absence of such a theory, an empirically chosen kernel width of $\sigma = 4 \times 10^{-3}$ is chosen. Comparison with reconstructions using different kernel sizes $\sigma$ served to verify that the statistical error in the reconstructed $\beta_t$ is small compared to the convergence error (due to finite $N$), for the range of $\tilde{E}$ values for which results are presented (e.g., for the Fig. 1 results a smaller kernel size $\sigma = 5 \times 10^{-4}$ was used, with no significant difference between the reconstructions). The range of values of $\tilde{E}$ (here approximately $-0.2 \leqslant \tilde{E} \leqslant 0.1$) for which statistical convergence is possible is limited by the central region in which most samples $\{\tilde{E}_i\}$ are located. An alternative method for sampling outside of the central region has been used [21]; however, it is unclear whether there is an associated bias, and there is no obvious means of estimating its magnitude.

Figure 2 shows the resulting comparison between the theoretical predictions [Eq. (44), solid curves] and statistical estimates [from Eqs. (47) and (48), broken curves] for $\beta_t(\tilde{E})$. There is good agreement for both domains, except at relatively low energies, where the theoretical prediction is higher. Statistical calculations with lower $N$ (not shown) suggest that the remaining discrepancy with (44) is partially a convergence (finite-$N$) issue, although bias in the statistical estimate due to the finite kernel size begins to make a small contribution to the error at the edges of the plotted range. Also plotted in Fig. 2 is the Edwards-Taylor [17] ($\tilde{E} \to -\infty$) estimate (31), which is seen to be inaccurate throughout the range in which statistical convergence is possible.

### C. Verification by direct numerical simulation

The theory of Sec. III is relevant to the dynamical system (1) only under the ergodic hypothesis, i.e., that long-time averages and ensemble averages (11) are equivalent. However, numerical calculations [24] have cast doubt on the validity of the ergodic hypothesis, at least for relatively low numbers of vortices ($N = 6$). Consequently, it is prudent to test the predictions of Sec. III using time averages of quantities obtained from dynamical integrations of (1), in addition to the verification against the statistical sampling of the microcanonical ensemble described above.

The equations of motion (1), with $N = 100$ vortices, are integrated numerically by first transforming into the circular image domain [1]. An adaptive time-stepping algorithm, with an advancement criterion based upon convergence of final vortex positions over a fixed time interval, is used to update vortex positions. Further details of the integration method and numerical parameters used are given elsewhere [25]. For each of the two Neumann oval domains, integrations are performed for 11 different energy levels, evenly spaced between $\tilde{E} = -0.15$ and $\tilde{E} = 0.1$. Initial conditions are generated randomly using the algorithm described in Sec. IV B. The adaptive time-stepping algorithm ensures that the Hamiltonian is conserved during these simulations up to an accuracy of six significant figures.

For each energy level, eight integrations of $1000N$ time units are performed. The reason that more than one integration per energy level is necessary is that the time-averaged statistics are found to converge only very slowly. Time averages of longer integrations ($10\,000N$ time units) are not found to be entirely independent of initial conditions, indicating that ergodicity is not attained on time scales that can be easily accessed by numerical simulations, although the system (with $N = 100$) may be ergodic on longer time scales. As a compromise between strict time averaging and ensemble averaging, therefore, the results presented below will be the mean and standard deviation of the small ensemble of time averages obtained from the eight dynamical runs at each energy level.

In order to compare the results of the dynamical runs with the theory and statistical calculations, it is necessary to look beyond the thermodynamic inverse temperature $\beta_t(\tilde{E})$, because $\beta_t(\tilde{E})$ cannot easily be estimated from dynamical runs at fixed $\tilde{E}$. Instead, the quantities of interest will be the projections of the vorticity fluctuation function $\omega_2$ onto the vorticity modes $\Phi_j$ ($j = 1,2,3\ldots$). By defining the projections

$$A_{jk} = \int_{\mathcal{D}^2} \omega_2(\boldsymbol{x},\boldsymbol{x}')\Phi_j(\boldsymbol{x})\Phi_k(\boldsymbol{x}')d\boldsymbol{x}\,d\boldsymbol{x}', \tag{49}$$

from the asymptotics introduced above it follows that

$$\lim_{N\to\infty} N A_{jk} = \rho_0 \begin{cases} a_{jj}, & j = k, \\ 0, & j \neq k, \end{cases}$$

with the theoretical result for the $a_{jj}$ given by (45).

To calculate the diagonal projection coefficients $\{A_{jj}\}$ associated with a particular vorticity mode $\Phi_j$, note that inserting the definition (13) into (49) leads to

$$A_{jj} = \langle \Omega_j^2 \rangle - \langle \Omega_j \rangle^2 - (1/N)\langle R_j \rangle. \tag{50}$$

Here angle brackets can be interpreted as either ensemble averages (for the statistical verification) or time averages (for the dynamical verification), and

$$\Omega_j = \int_{\mathcal{D}} \omega(\boldsymbol{x})\Phi_j(\boldsymbol{x})d\boldsymbol{x} = \sum_{i=1}^{N} \Gamma_i \Phi_j(\boldsymbol{x}_i), \tag{51}$$

$$R_j = \int_{\mathcal{D}} \rho(\boldsymbol{x})\Phi_j(\boldsymbol{x})^2 d\boldsymbol{x} = \frac{1}{N}\sum_{i=1}^{N} \Phi_j(\boldsymbol{x}_i)^2 \tag{52}$$

are the projection of the vorticity field $\omega$ onto the $j$th vorticity mode and the projection of the vortex density $\rho$ onto the square of the $j$th vorticity mode, respectively. In the limit $N \to \infty$, $\langle \rho \rangle = \rho_1 = \rho_0 + O(1/N)$ and therefore $R_j \to \rho_0$ at leading order. It follows that, as $N \to \infty$, the variance of $\Omega_j$ satisfies

$$\lim_{N\to\infty} \mathrm{Var}(\Omega_j) = \frac{\rho_0}{N}(a_{jj} + 1), \tag{53}$$

In other words, the coefficients $\{a_{jj}\}$ are linearly related to the variance of the vorticity field with respect to each vorticity mode, providing a simple interpretation of their meaning. Further meaning is provided by the energy equation in the form (39), from which it is clear that the energy trapped in each mode is given by $-a_{jj}/2\beta_j$, a quantity that can be positive or negative.

Based on the relationship (53), a comparison between the theoretical predictions for and statistical and dynamical calculations of the variance associated with the first four vorticity modes for the $q = 0.3$ Neumann oval (illustrated) is shown in Fig. 3. The left panels show contour plots of the vorticity modes $\Phi_j(\boldsymbol{x})$ for $j = 1$, 2, 3, and 4, plotted underneath the corresponding DITs ($\beta_j$). The right panels compare theoretical, statistical, and dynamical Var$(\Omega_j)$ (scaled by $\rho_0/N$). The theoretical predictions $a_{jj}(\tilde{E}) + 1$ (solid curves) from (45) are plotted against statistical estimates of the ensemble average Var$(\Omega_j)$ (broken curves). The gray points show Var$(\Omega_j)$ in the dynamical runs, interpreted as variance in time, and averaged over the set of eight runs performed at each energy level $\tilde{E}$. (Note that the theoretical long-time mean $\langle\Omega_j\rangle = 0$ is used as the basis of the dynamical run calculations.) The error bars on the gray points show the standard deviation among the eight runs. Good agreement is evident among the theoretical curves, statistical data, and dynamical runs. Finally, the dotted lines, plotted at Var$(\Omega_j)\times N/\rho_0 = 1$, show the level at which the fluctuations associated with the vorticity mode in question are neutral with respect to the system's energy.

Figure 4 shows the corresponding picture for the $q = 0.8$ Neumann oval. Good agreement between theory and data is again evident. Some interesting differences between the two domains are apparent in the energy partitioning. In the $q = 0.3$ domain the energy contained in the first three vorticity modes (proportional to $a_{jj}/\beta_j$), each of which have tightly clustered DITs, is seen to increase near linearly with the total energy. The fourth mode, by contrast, saturates at low energy. In the $q = 0.8$ domain the situation is quite different. There, as total energy $\tilde{E}$ increases, all vorticity modes saturate at low energy except for the first, which increases linearly at the same rate as $\tilde{E}$. The only possible reason for the different behavior between the domains is the different distributions of the DITs, which in the $q = 0.8$ domain are well separated, unlike in the $q = 0.3$ case.

Figure 5 shows the time evolution of the vorticity projections $\Omega_j(t)$, for the first four vorticity modes ($j = 1,2,3,4$), during four different numerical simulations. The upper panels contrast the $q = 0.3$ and $q = 0.8$ Neumann ovals at negative energies ($\tilde{E} = -0.1$). The striking feature of these time series, which cannot be anticipated from the analysis above, is the comparatively long time scales associated with $\Omega_1(t)$ in the $q = 0.8$ oval. Otherwise, the variance of $\Omega_j$ among the four modes is comparable for each domain, as could be anticipated at this energy ($\tilde{E} = -0.1$) from the predictions of Figs. 3 and 4 [since Var$(\Omega_j) \sim a_{jj} + 1$].

The lower panels show the same time series for simulations at a positive value of the energy ($\tilde{E} = 0.05$). It is evident immediately that the variance in $\Omega_j$, and hence the energy, associated with each mode is greatly increased. In the $q = 0.3$ domain the first three modes have comparable variances, whereas for the $q = 0.8$ the first mode clearly contains most of the energy. Again, this is consistent with Figs. 3 and 4. Not predicted by Figs, 3 and 4, however, are the changes in the time scales associated with each mode. In the $q = 0.3$ domain, the first three modes clearly exhibit variability on time scales $\sim 50N$, whereas for the fourth mode the persistence time scale is an order of magnitude shorter. In the $q = 0.8$ domain, modes 2, 3, and 4 exhibit relatively short time scales, not much longer than the eddy turnover time. By contrast the first mode projection $\Omega_1(t)$ changes sign only once in the $T = 1000N$ simulation, indicating that the system is prone to oscillations between metastable states with large positive or

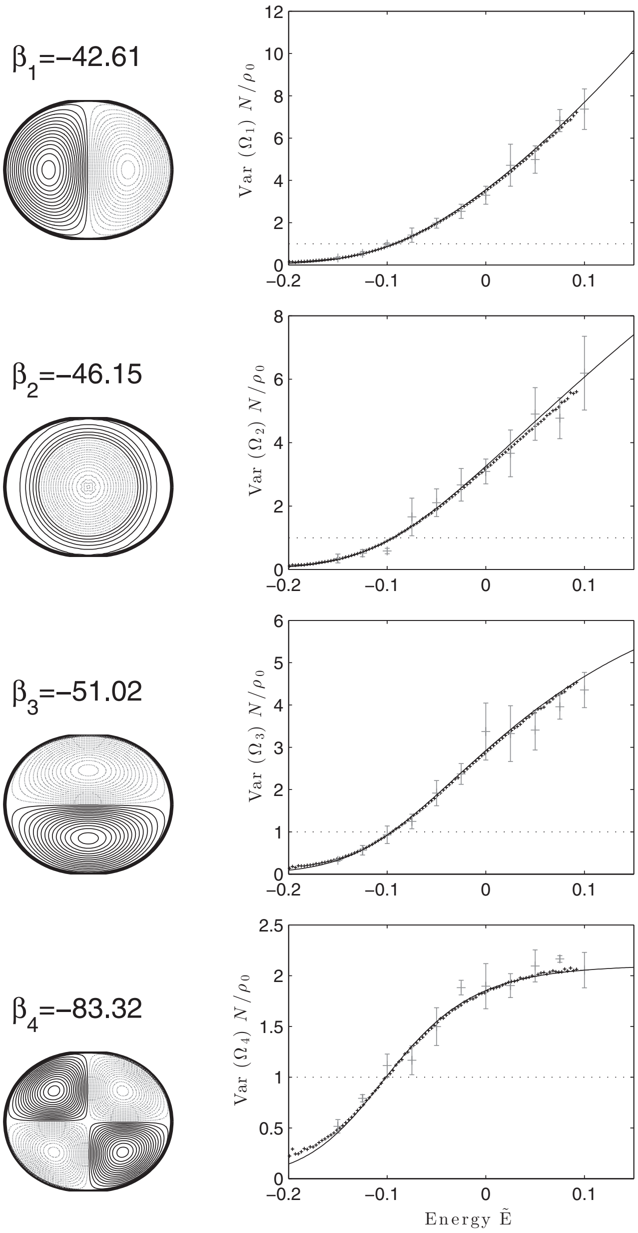

FIG. 3. Left panels: Contour plots of the first four vorticity modes $\Phi_j(\boldsymbol{x})$ ($j = 1,2,3,4$) and the corresponding DITs $\beta_j$ for the $q = 0.3$ Neumann oval domain. Positive contours are black and negative contours are gray. Right panels: The theoretical ($N \to \infty$) amplitude $a_{jj}(\tilde{E})$ of the projection of the vorticity fluctuations onto the corresponding vorticity mode $\Phi_j$ (solid curves), together with the statistical estimate of the microcanonical ensemble mean of the corresponding projection $NA_{jj}/\rho_0$ for $N = 100$ (broken curves), and the same quantity for the dynamical runs (gray points with error bars). For the dynamical runs an average over the time means of 8 runs of $1000N$ time units is taken, with the error bars showing the standard deviation in those time means.

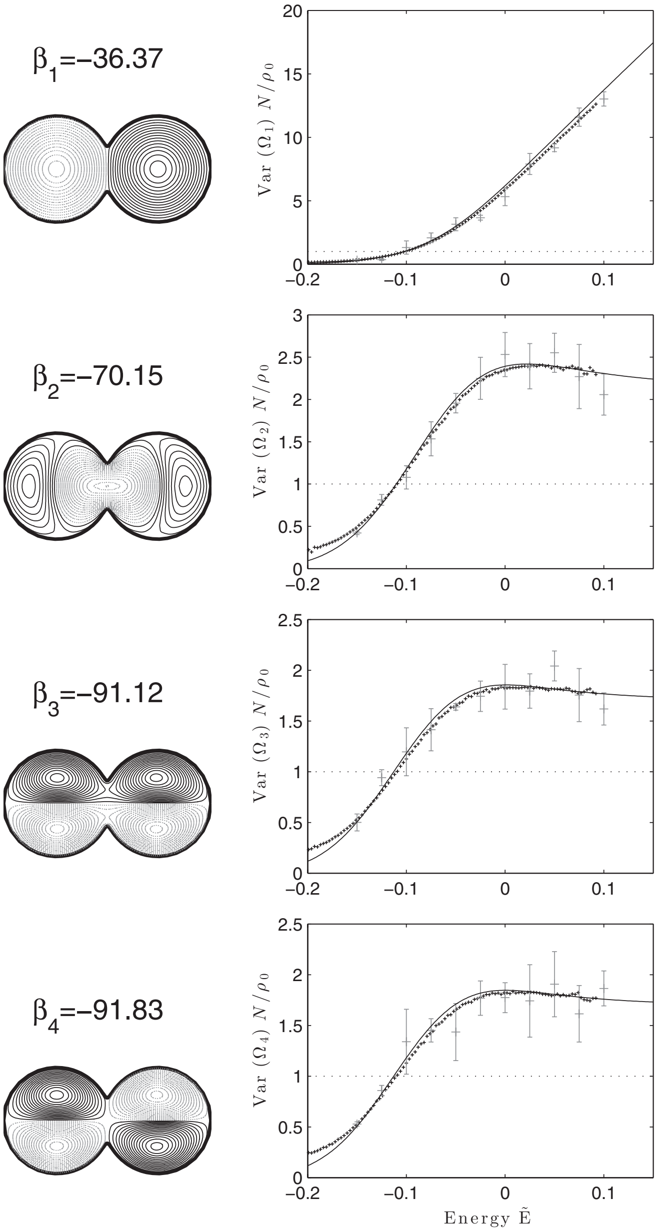

FIG. 4. Same as Fig. 3 but for the $q = 0.8$ Neumann oval domain.

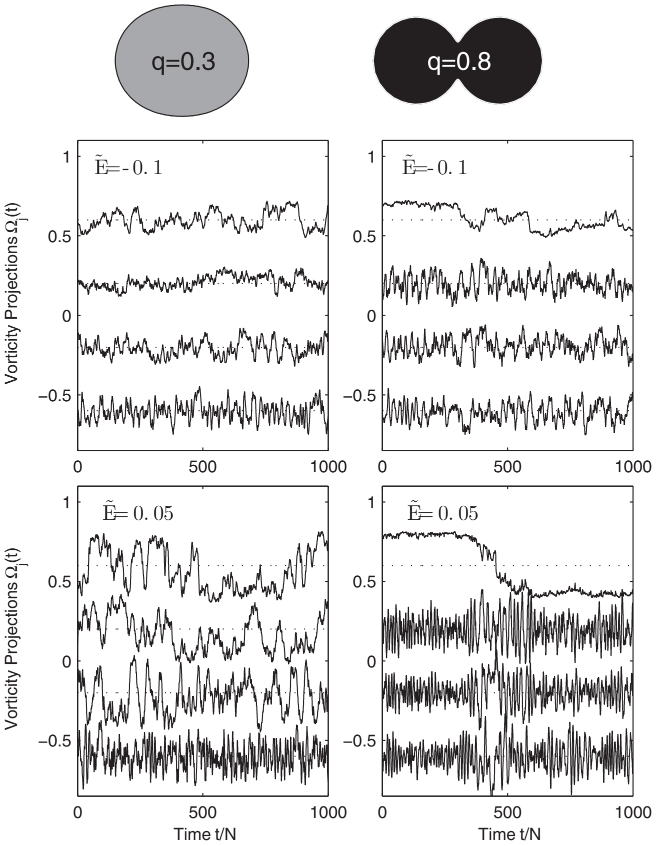

FIG. 5. Time series of the projections $\Omega_j(t)$ of the vorticity field $\omega(\boldsymbol{x})$ onto the vorticity modes $\Phi_j(\boldsymbol{x})$ for the first four vorticity modes $j = 1,2,3,4$ (see left panels of Figs. 3 and 4). Left panels show results for the Neumann oval with $q = 0.3$ and right panels show results for $q = 0.8$. Upper panels show results at negative energy $\tilde{E} = -0.1$ and lower panels show those at positive energy $\tilde{E} = +0.05$. In each panel $\Omega_1(t)$ to $\Omega_4(t)$ are plotted as solid curves with offsets of $+0.6$, $+0.2$, $-0.2$, and $-0.6$, respectively. Dotted lines show the zero line for each curve.

negative $\Omega_1(t)$. It is interesting to note the behavior during the period $t = 400N$ to $550N$ during which the sign of $\Omega_1(t)$ changes. The variance of $\Omega_2$, $\Omega_3$, and $\Omega_4$ is significantly greater during this period, as the energy stored in mode 1 is temporarily shared among the remaining modes.

Integrations in the $q = 0.8$ domain at higher energies (not shown) show that the system often remains in one such metastable state, diagnosed by $\Omega_1(t)$ being strongly positive or negative, for the duration of the integration. As energy increases the time scales for such oscillations evidently become progressively longer. This is consistent with the idea that, as energy increases, a symmetry-breaking Bose condensation [26] takes place; i.e., a mean flow becomes established because one metastable state is selected at random by the system, which then persists indefinitely. The mean flow situation is best described by the hydrodynamic scaling and the mean flow itself by the solution to the sinh-Poisson equation.

The picture emerging from the results above is that a significant qualitative difference can be expected between the dynamics of domains with their first few DITs closely clustered (e.g., the $q = 0.3$ oval) and those with a significant separation between their first and second DITs (e.g., the $q = 0.8$ oval). In the former domains, as total energy increases, the energy in the system is (largely) partitioned among the modes associated with the clustered DITs, and a persistent, symmetry-breaking mean flow is slow to emerge. In the latter domains, by contrast, energy becomes concentrated in the first vorticity mode, and as energy increases the system spends progressively longer times in metastable states. For a system with a fixed number of vortices $N$, the value of the energy above which a persistent mean flow is established will be substantially higher for domains with clustered DITs. The present results therefore provide a simple qualitative guide to the likely range of applicability of the sinh-Poisson equation in different domains.

## V. CONCLUSIONS

Equations (41) and (44) are analytical expressions for the limiting form, as the number of vortices $N \to \infty$, of the thermodynamic density of states $W_t(\tilde{E})$ and inverse temperature $\beta_t(\tilde{E})$ of a neutral point-vortex gas. Both formulas are functions of $\tilde{E} = NE$, the thermodynamic (scaled) energy, and, consequently, for a gas with finite $N$, lead to accurate predictions for states with low (positive or negative) energies in which the distribution of vortices is close to uniform. The statistical results of Fig. 1, confirming the results of earlier work [10], illustrate that specifying that thermodynamic energy remains constant as $N \to \infty$ corresponds to the "central limit" for the vortex gas, whereas the more widely studied hydrodynamic or sinh-Poisson limit ($N \to \infty$, $E =$ constant) can be viewed as a large-deviation result for positive $E$. Interestingly, there does not appear to be a corresponding theory for negative $E$.

A notable feature of (41) and (44) is that the structure of both curves depends only on the domain inverse temperatures calculated from the eigenvalue problem (34). The DITs themselves depend only on the shape, and not on the size, of the domain $\mathcal{D}$. The domain size independence is expected because the governing equations (1) are themselves invariant under a rescaling of $\mathcal{D}$. It follows that the influence of the domain on the physics of the system cannot be scaled away by taking a "true" thermodynamic limit ($|\mathcal{D}| \to \infty$ as $N \to \infty$) and that no domain-independent equation of state exists for the vortex gas. The long-range interactions in the vortex system have no associated length scale that limits the influence of the boundary (or equivalently the associated "image" vortices, which enter at leading order in the dynamics). Because the influence of the domain remains central to the dynamics, an interesting problem in spectral theory concerns how exactly the geometry of $\mathcal{D}$ controls the distribution of DITs and thus $\beta_t(\tilde{E})$. It is worth emphasizing that the doubly-periodic geometry, so widely used in the study of two-dimensional turbulence, is a *particular* domain $\mathcal{D}$ with its own (highly degenerate) distribution of DITs.

A relatively unexplored aspect of considerable interest is the transition, in a gas with finite $N$, between behavior best described by the thermodynamic scaling and the vorticity fluctuation equation (32) and behavior described by the hydrodynamic scaling and the sinh-Poisson equation (8) [5]. The latter regime is characterized by the spontaneous, symmetry-breaking emergence of a mean circulation in the domain, a phenomenon which has been described in the two-dimensional turbulence literature [26] as Bose condensation. The transition between the two behaviors involves, as is typical of phase transitions, a rapid increase in the share of the energy and decorrelation time scale associated with fluctuations of a particular type or structure. The results of Figs. 3–5 show clearly that the relevant structure for the vortex gas is that of the leading vorticity mode. An intriguing qualitative result, evident from examination of (45), is that the extent to which energy becomes trapped in this structure, as $\tilde{E}$ increases, is sensitive to the separation between the first few DITs. The question of whether the apparent significance of the leading vorticity mode can be reconciled with sinh-Poisson results will be studied in detail in future work. As noted by PL76 [15] it is a question that must involve asymptotic matching between the thermodynamic scaling results as $\tilde{E} \to \infty$ and hydrodynamic scaling results as $E \to 0$. Progress in the latter limit has been made by Chavanis and Sommeria [27], who investigated the Miller-Robert-Sommeria [28–30] finite-vorticity extension of the point-vortex statistical theory, in a low-energy regime that they referred to as the "strong mixing limit." The statistical equilibria in this limit were found to be determined by an eigenvalue problem that, after a transformation, can be shown to be equivalent to (34) above.

The discovery of the natural basis of vorticity modes raises the possibility of a more complete statistical description of the neutral point-vortex gas. In particular, temporal correlations can be investigated using recently derived kinetic equations (see, e.g., Chavanis [31]). It is also noteworthy that the methodology described here also allows the statistics of a range of related systems, e.g., quasi-geostrophic vorticity dynamics [32], to be solved in arbitrary bounded domains.

## ACKNOWLEDGEMENT

T.L.A. acknowledges the Department of Mathematics at University College London for providing funding for research through a departmental teaching assistant fellowship.

## APPENDIX A: DERIVATION OF THE SECOND-ORDER CUMULANT EQUATIONS

In this Appendix the missing detail in the derivation of (19) and (20) is supplied and a full account of the derivation of the second-order cumulant equations (21)–(23) is given.

The missing detail needed to obtain (19) and (20) is the equation for $\nabla p_-$, which is straightforward to obtain following the method used for (18):

$$\nabla p_-(\boldsymbol{x}) = (\partial_{\tilde{E}} + \beta)\left(\frac{1}{2}\int_{\mathcal{D}} \nabla G(\boldsymbol{x},\boldsymbol{x}')[p_{--}(\boldsymbol{x},\boldsymbol{x}') - p_{-+}(\boldsymbol{x},\boldsymbol{x}')]d\boldsymbol{x}' - \frac{1}{N}\int_{\mathcal{D}} \nabla G(\boldsymbol{x},\boldsymbol{x}')p_{--}(\boldsymbol{x},\boldsymbol{x}')d\boldsymbol{x}' + \frac{1}{2N}\nabla g(\boldsymbol{x},\boldsymbol{x})p_-(\boldsymbol{x})\right). \tag{A1}$$

Equation (19) follows from taking $1/2 \times$ [(18)−(A1)], and (20) follows from taking $1/2 \times$ [(18) + (A1)].

Careful application of the same procedure to the marginal density $p_{++}$ leads to

$$\begin{aligned}\nabla p_{++}(\boldsymbol{x},\boldsymbol{x}') = (\partial_{\tilde{E}} + \beta)\Bigg(&\frac{1}{2}\int_{\mathcal{D}} \nabla G(\boldsymbol{x},\boldsymbol{x}'')[p_{+++}(\boldsymbol{x},\boldsymbol{x}',\boldsymbol{x}'') - p_{++-}(\boldsymbol{x},\boldsymbol{x}',\boldsymbol{x}'')]d\boldsymbol{x}''\\ &-\frac{2}{N}\int_{\mathcal{D}} \nabla G(\boldsymbol{x},\boldsymbol{x}'')p_{+++}(\boldsymbol{x},\boldsymbol{x}',\boldsymbol{x}'')d\boldsymbol{x}'' + \frac{1}{N}\nabla G(\boldsymbol{x},\boldsymbol{x}')p_{++}(\boldsymbol{x},\boldsymbol{x}') + \frac{1}{2N}\nabla g(\boldsymbol{x},\boldsymbol{x})p_{++}(\boldsymbol{x},\boldsymbol{x}')\Bigg).\end{aligned} \tag{A2}$$

Similarly,

$$\nabla p_{+-}(\boldsymbol{x},\boldsymbol{x}') = (\partial_{\tilde{E}} + \beta)\bigg(\frac{1}{2}\int_{\mathcal{D}} \nabla G(\boldsymbol{x},\boldsymbol{x}'')[p_{+-+}(\boldsymbol{x},\boldsymbol{x}',\boldsymbol{x}'') - p_{+--}(\boldsymbol{x},\boldsymbol{x}',\boldsymbol{x}'')]d\boldsymbol{x}'' - \frac{1}{N}\int_{\mathcal{D}} \nabla G(\boldsymbol{x},\boldsymbol{x}'')[p_{+-+}(\boldsymbol{x},\boldsymbol{x}',\boldsymbol{x}'') - p_{+--}(\boldsymbol{x},\boldsymbol{x}',\boldsymbol{x}'')]d\boldsymbol{x}'' - \frac{1}{N}\nabla G(\boldsymbol{x},\boldsymbol{x}')p_{+-}(\boldsymbol{x},\boldsymbol{x}') + \frac{1}{2N}\nabla g(\boldsymbol{x},\boldsymbol{x})p_{+-}(\boldsymbol{x},\boldsymbol{x}')\bigg), \tag{A3}$$

$$\nabla p_{-+}(\boldsymbol{x},\boldsymbol{x}') = (\partial_{\tilde{E}} + \beta)\bigg(-\frac{1}{2}\int_{\mathcal{D}} \nabla G(\boldsymbol{x},\boldsymbol{x}'')[p_{-++}(\boldsymbol{x},\boldsymbol{x}',\boldsymbol{x}'') - p_{-+-}(\boldsymbol{x},\boldsymbol{x}',\boldsymbol{x}'')]d\boldsymbol{x}'' + \frac{1}{N}\int_{\mathcal{D}} \nabla G(\boldsymbol{x},\boldsymbol{x}'')[p_{-++}(\boldsymbol{x},\boldsymbol{x}',\boldsymbol{x}'') - p_{-+-}(\boldsymbol{x},\boldsymbol{x}',\boldsymbol{x}'')]d\boldsymbol{x}'' - \frac{1}{N}\nabla G(\boldsymbol{x},\boldsymbol{x}')p_{-+}(\boldsymbol{x},\boldsymbol{x}') + \frac{1}{2N}\nabla g(\boldsymbol{x},\boldsymbol{x})p_{-+}(\boldsymbol{x},\boldsymbol{x}')\bigg), \tag{A4}$$

$$\nabla p_{--}(\boldsymbol{x},\boldsymbol{x}') = (\partial_{\tilde{E}} + \beta)\bigg(\frac{1}{2}\int_{\mathcal{D}} \nabla G(\boldsymbol{x},\boldsymbol{x}'')[p_{---}(\boldsymbol{x},\boldsymbol{x}',\boldsymbol{x}'') - p_{--+}(\boldsymbol{x},\boldsymbol{x}',\boldsymbol{x}'')]d\boldsymbol{x}'' - \frac{2}{N}\int_{\mathcal{D}} \nabla G(\boldsymbol{x},\boldsymbol{x}'')p_{---}(\boldsymbol{x},\boldsymbol{x}',\boldsymbol{x}'')d\boldsymbol{x}'' + \frac{1}{N}\nabla G(\boldsymbol{x},\boldsymbol{x}')p_{--}(\boldsymbol{x},\boldsymbol{x}') + \frac{1}{2N}\nabla g(\boldsymbol{x},\boldsymbol{x})p_{--}(\boldsymbol{x},\boldsymbol{x}')\bigg). \tag{A5}$$

To obtain the equation for $\nabla\omega_2$ take

$$\frac{1}{4}([(\mathrm{A2}) - \mathrm{p}_+(\boldsymbol{x}')(18)] - [(\mathrm{A3}) - \mathrm{p}_-(\boldsymbol{x}')(18)] - [(\mathrm{A4}) - \mathrm{p}_+(\boldsymbol{x}')(\mathrm{A1})] + [(\mathrm{A5}) - \mathrm{p}_-(\boldsymbol{x}')(\mathrm{A1})]) - \frac{1}{2\mathrm{N}}[(\mathrm{A2}) + (\mathrm{A5})]$$

and for $\nabla c_2$

$$\frac{1}{4}([(\mathrm{A2}) - \mathrm{p}_+(\boldsymbol{x}')(18)] - [(\mathrm{A3}) - \mathrm{p}_-(\boldsymbol{x}')(18)] + [(\mathrm{A4}) - \mathrm{p}_+(\boldsymbol{x}')(\mathrm{A1})] - [(\mathrm{A5}) - \mathrm{p}_-(\boldsymbol{x}')(\mathrm{A1})]) - \frac{1}{2\mathrm{N}}[(\mathrm{A2}) - (\mathrm{A5})]$$

with a similar calculation for $\nabla\rho_2$ leading to (23). In the latter case, the second-order cumulant

$$\phi_2(\boldsymbol{x},\boldsymbol{x}') = \int_{\mathcal{D}} c_2(\boldsymbol{x},\boldsymbol{x}'')G(\boldsymbol{x}'',\boldsymbol{x}')d\boldsymbol{x}'' = \langle[\rho(\boldsymbol{x}) - \rho_1(\boldsymbol{x})][\psi(\boldsymbol{x}') - \psi_1(\boldsymbol{x}')]\rangle - \frac{1}{N}\omega_1(\boldsymbol{x})G(\boldsymbol{x},\boldsymbol{x}')$$

has been introduced. The third-order desingularized cumulants are defined to be

$$\begin{aligned}
\omega_3(\boldsymbol{x},\boldsymbol{x}',\boldsymbol{x}'') = {} & \langle[\omega(\boldsymbol{x}) - \omega_1(\boldsymbol{x})][\omega(\boldsymbol{x}') - \omega_1(\boldsymbol{x}')][\omega(\boldsymbol{x}'') - \omega_1(\boldsymbol{x}'')]\rangle \\
& - \frac{1}{N}(\delta(\boldsymbol{x}'' - \boldsymbol{x})c_2(\boldsymbol{x},\boldsymbol{x}') + \delta(\boldsymbol{x} - \boldsymbol{x}')c_2(\boldsymbol{x}',\boldsymbol{x}'') + \delta(\boldsymbol{x}' - \boldsymbol{x}'')c_2(\boldsymbol{x}'',\boldsymbol{x})) + \frac{2}{N^2}\delta(\boldsymbol{x}' - \boldsymbol{x})\delta(\boldsymbol{x}'' - \boldsymbol{x})\omega_1(\boldsymbol{x}) \\
c_3(\boldsymbol{x},\boldsymbol{x}',\boldsymbol{x}'') = {} & \langle[\rho(\boldsymbol{x}) - \rho_1(\boldsymbol{x})][\omega(\boldsymbol{x}') - \omega_1(\boldsymbol{x}')][(\omega(\boldsymbol{x}'') - \omega_1(\boldsymbol{x}'')]\rangle \\
& - \frac{1}{N}(\delta(\boldsymbol{x}' - \boldsymbol{x}'')\rho_2(\boldsymbol{x},\boldsymbol{x}') + \delta(\boldsymbol{x} - \boldsymbol{x}')\omega_2(\boldsymbol{x},\boldsymbol{x}'') + \delta(\boldsymbol{x} - \boldsymbol{x}'')\omega_2(\boldsymbol{x},\boldsymbol{x}')) + \frac{2}{N^2}\delta(\boldsymbol{x}' - \boldsymbol{x})\delta(\boldsymbol{x}'' - \boldsymbol{x})\rho_1(\boldsymbol{x})
\end{aligned}$$

and can be introduced into the calculation by means of the identities

$$\begin{aligned}
& \omega_3(\boldsymbol{x},\boldsymbol{x}',\boldsymbol{x}'') + \omega_1(\boldsymbol{x})\omega_2(\boldsymbol{x}',\boldsymbol{x}'') + \omega_1(\boldsymbol{x}')\omega_2(\boldsymbol{x}'',\boldsymbol{x}) + \omega_1(\boldsymbol{x}'')\omega_2(\boldsymbol{x},\boldsymbol{x}') + \omega_1(\boldsymbol{x})\omega_1(\boldsymbol{x}')\omega_1(\boldsymbol{x}'') \\
& \quad = \frac{1}{8}[p_{+++}(\boldsymbol{x},\boldsymbol{x}',\boldsymbol{x}'') - p_{[++-]}(\boldsymbol{x},\boldsymbol{x}',\boldsymbol{x}'') + p_{[--+]}(\boldsymbol{x},\boldsymbol{x}',\boldsymbol{x}'') - p_{---}(\boldsymbol{x},\boldsymbol{x}',\boldsymbol{x}'')] \\
& \quad - \frac{1}{4N}[3p_{+++}(\boldsymbol{x},\boldsymbol{x}',\boldsymbol{x}'') - p_{[++-]}(\boldsymbol{x},\boldsymbol{x}',\boldsymbol{x}'') + p_{[--+]}(\boldsymbol{x},\boldsymbol{x}',\boldsymbol{x}'') - 3p_{---}(\boldsymbol{x},\boldsymbol{x}',\boldsymbol{x}'')] \\
& \quad + \frac{1}{N^2}[p_{+++}(\boldsymbol{x},\boldsymbol{x}',\boldsymbol{x}'') - p_{---}(\boldsymbol{x},\boldsymbol{x}',\boldsymbol{x}'')], \\
& c_3(\boldsymbol{x},\boldsymbol{x}',\boldsymbol{x}'') + \rho_1(\boldsymbol{x})\omega_2(\boldsymbol{x}',\boldsymbol{x}'') + \omega_1(\boldsymbol{x}')c_2(\boldsymbol{x},\boldsymbol{x}'') + \omega_1(\boldsymbol{x}'')c_2(\boldsymbol{x},\boldsymbol{x}') + \rho_1(\boldsymbol{x})\omega_1(\boldsymbol{x}')\omega_1(\boldsymbol{x}'') \\
& \quad = \frac{1}{8}[p_{+++}(\boldsymbol{x},\boldsymbol{x}',\boldsymbol{x}'') + p_{(-++)}(\boldsymbol{x},\boldsymbol{x}',\boldsymbol{x}'') + p_{(+--)}(\boldsymbol{x},\boldsymbol{x}',\boldsymbol{x}'') + p_{---}(\boldsymbol{x},\boldsymbol{x}',\boldsymbol{x}'')] \\
& \quad - \frac{1}{4N}[3p_{+++}(\boldsymbol{x},\boldsymbol{x}',\boldsymbol{x}'') + p_{(-++)}(\boldsymbol{x},\boldsymbol{x}',\boldsymbol{x}'') + p_{(+--)}(\boldsymbol{x},\boldsymbol{x}',\boldsymbol{x}'') + 3p_{---}(\boldsymbol{x},\boldsymbol{x}',\boldsymbol{x}'')] \\
& \quad + \frac{1}{N^2}[p_{+++}(\boldsymbol{x},\boldsymbol{x}',\boldsymbol{x}'') - p_{---}(\boldsymbol{x},\boldsymbol{x}',\boldsymbol{x}'')],
\end{aligned}$$

where the shorthand $p_{[++-]} = p_{++-} + p_{-++} + p_{+-+}$ and $p_{(-++)} = p_{-++} - p_{+-+} - p_{++-}$ has been used.

## APPENDIX B: GREEN'S FUNCTIONS FOR CONFORMAL DOMAINS

For the analysis in this work to be widely applicable, it is necessary to be able to find explicit formulas for the Green's functions $G(\boldsymbol{x},\boldsymbol{x}')$ in a wide range of domains $\mathcal{D}$. Results for many simple geometries are well known; for example,

$$G_c(\boldsymbol{x},\boldsymbol{x}') = \frac{1}{2\pi}\log|\boldsymbol{x}-\boldsymbol{x}'| - \frac{1}{4\pi}\log(1-2\boldsymbol{x}\cdot\boldsymbol{x}'+|\boldsymbol{x}|^2|\boldsymbol{x}'|^2) \tag{B1}$$

is the Green's function for the unit circle [11]. Other authors [10] have used Ewald summation to add the contributions from infinitely many images to obtain results for regular parallelograms. Here, more general formulas are presented [1,9], allowing Green's functions to be found for all domains $\mathcal{D}$ for which an explicit conformal map exists between $\mathcal{D}$ and the unit circle.

The method for finding the functions $G(\boldsymbol{x},\boldsymbol{x}')$ and $g(\boldsymbol{x},\boldsymbol{x})$ appearing in the Hamiltonian (2) in this case is as follows. Consider the conformal map $Z = f(z)$ that maps the simply connected domain $\mathcal{D}$ in the $z$ plane to the unit disk in the $Z$ plane. The usual correspondence between $\mathbb{C}$ and $\mathbb{R}^2$ is taken to hold, so that $Z = X + \mathrm{i}Y \in \mathbb{C}$ is identified with $\boldsymbol{X} = (XY)^T \in \mathbb{R}^2$, and likewise $z = x + \mathrm{i}y$ with $\boldsymbol{x}$. The important point, outlined, e.g., in Newton [1], is that the Green's function itself is preserved by the mapping; hence in $\mathcal{D}$

$$G(\boldsymbol{x},\boldsymbol{x}') = G_c(\boldsymbol{f}(\boldsymbol{x}),\boldsymbol{f}(\boldsymbol{x}')), \tag{B2}$$

with the vector-valued function $\boldsymbol{X} = \boldsymbol{f}(\boldsymbol{x})$ simply being the $\mathbb{R}^2$ expression of $Z = f(z)$.

A subtlety arises in the evaluation of the Robin function $g(\boldsymbol{x},\boldsymbol{x})$ appearing in the Hamiltonian formula. Careful evaluation of the limit $\boldsymbol{x}' \to \boldsymbol{x}$ leads to

$$\begin{aligned} g(\boldsymbol{x},\boldsymbol{x}) &= g_c(\boldsymbol{f}(\boldsymbol{x}),\boldsymbol{f}(\boldsymbol{x})) + \frac{1}{2\pi}\log|f'(z)| \\ &= g_c(\boldsymbol{f}(\boldsymbol{x}),\boldsymbol{f}(\boldsymbol{x})) - \frac{1}{2\pi}\log|F'(Z)|, \end{aligned} \tag{B3}$$

where the final expression, given in terms of the inverse map to $Z = f(z)$, namely, $z = F(Z)$, allows evaluation using the circular domain coordinates only. Evaluation of the Hamiltonian using these expressions for $G$ and $g$ leads to the well-known Kirchoff-Routh formula [1].

## APPENDIX C: NUMERICAL SOLUTION OF THE VORTICITY MODE EIGENVALUE PROBLEM (34)

The numerical method used to solve (34) is based on standard spectral techniques [20]. Note first that, upon taking the Laplacian, (34) can be written as

$$\nabla^2\Phi = \beta\rho_0\left(\Phi - \rho_0\int_{\mathcal{D}}\Phi\,d\boldsymbol{x}\right). \tag{C1}$$

The vorticity modes $\{\Phi_j(\boldsymbol{x}), j \geqslant 1\}$ also satisfy the integral condition (35); hence they also are solutions of

$$\nabla^2\Phi = \beta\rho_0\Phi. \tag{C2}$$

To define an eigenvalue problem from (C2), from which the vorticity modes can be found, it is necessary to supply appropriate boundary conditions. From the fact that $G(\boldsymbol{x},\boldsymbol{x}') = 0$ for $\boldsymbol{x}$ on $\partial\mathcal{D}$, it can be deduced that solutions of (34) satisfy

$$\Phi(\boldsymbol{x}) = \text{constant on } \partial\mathcal{D}. \tag{C3}$$

Further, integration of (C1) reveals that

$$\int_{\mathcal{D}}\nabla^2\Phi\,d\boldsymbol{x} = 0, \quad \text{or} \quad \oint_{\partial\mathcal{D}}\nabla\Phi\cdot\boldsymbol{n}\,ds = 0, \tag{C4}$$

where $\boldsymbol{n}$ is the unit normal to $\partial\mathcal{D}$. The two boundary conditions (C3) and (C4), which are easily interpreted physically as "no-normal flow" and "zero circulation," applied to (C2), generate a well-posed eigenvalue problem satisfied by the vorticity modes $\Phi_j(\boldsymbol{x})$ $(j \geqslant 1)$. It is to be emphasized that the resulting eigenvalue problem is distinct from those defined by pure Dirichlet or Neumann boundary conditions.

The eigenvalue problem (C2) + (C3) + (C4) is next transformed to the unit circle using the conformal map. In the circle domain, the problem transforms to

$$\nabla^2_X\Phi = \beta\rho_0|F'(Z)|^2\Phi,$$

[cf. Eq. (B3) above] with the boundary conditions unchanged. In the circle, standard techniques from Trefethen [20] can be used to form a discrete (matrix) Laplacian. The matrix Laplacian acts on a vector with entries consisting of $\Phi$ evaluated on a grid that consists of the Chebyshev points in the radial direction $(0 < R < 1)$ and is uniformly spaced in the azimuthal direction. A standard matrix eigenvalue solver is then used to find the eigenvalues (DITs) and eigenfunctions $\{\Phi_j\}$, which are then mapped back to $\mathcal{D}$. The method is spectrally accurate, and convergence to nine significant figures can typically be obtained using 39 radial and 40 azimuthal points.

---

[1] P. K. Newton, *The N-Vortex Problem: Analytical Techniques* (Springer-Verlag, New York, 2001).

[2] R. H. Kraichnan and D. Montgomery, Rep. Prog. Phys. **43**, 547 (1980).

[3] D. Montgomery, in *Mathematical and Physical Theory of Turbulence*, edited by J. Cannon and B. Shivamoggi (Taylor and Francis, London, 2006), Chap. 5, p. 192.

[4] G. L. Eyink and K. R. Sreenivasan, Rev. Mod. Phys. **78**, 87 (2006).

[5] G. Joyce and D. Montgomery, J. Plasma Phys. **10**, 107 (1973).

[6] C. F. Barenghi, R. J. Donnelly, and W. F. Vinen, *Quantized Vortex Dynamics and Superfluid Turbulence* (Springer-Verlag, Berlin, 2001).

[7] A. Campa, T. Dauxois, and S. Ruffo, Phys. Rep. **480**, 57 (2009).

[8] P.-H. Chavanis, in *Dynamics and Thermodynamics of Systems with Long Range Interactions*, Lecture Notes in Physics, Vol. 602, edited by T. Dauxois, S. Ruffo, E. Arimondo, and M. Wilkens (Springer, New York, 2002).

[9] C. C. Lin, Proc. Natl Acad. Sci. USA **27**, 570 (1941).
[10] L. J. Campbell and K. O'Neil, J. Stat. Phys. **65**, 495 (1991).
[11] O. Bühler, Phys. Fluids **14**, 2139 (2002).
[12] Details of the method of statistical estimation are given in Sec. IV. B. Compare also Figs. 1–5 of Campbell and O'Neil [10].
[13] J. Fröhlich and D. Ruelle, Commun. Math. Phys. **87**, 1 (1982).
[14] The conclusion of Frohlich and Ruelle [13] that there are no negative temperature states in the thermodynamic limit is strictly correct in the textbook thermodynamic limit they consider, but it is unhelpful. Their conclusion is a direct consequence of the logarithmic shift in the energy as the domain size increases, meaning that the textbook limit they examine is equivalent to taking $\tilde{E} \to \text{constant} - (1/4\pi)\log N$ as $N \to \infty$ instead of $\tilde{E} = \text{constant}$ as $N \to \infty$ in the thermodynamic scaling limit considered here.
[15] Y. B. Pointin and T. S. Lundgren, Phys. Fluids **19**, 1459 (1976).
[16] M. K.-H. Kiessling, Lett. Math. Phys. **34**, 49 (1995).
[17] S. F. Edwards and J. B. Taylor, Proc. R. Soc. A **336**, 257 (1974).
[18] L. Debnath and P. Mikusiński, *Introduction to Hilbert Spaces with Applications*, 3rd ed. (Elsevier, New York, 2005).
[19] A change in domain size $\mathcal{D} \to \alpha\mathcal{D}$ results in a shift $\tilde{E}_0 \to \tilde{E}_0 - (1/4\pi)\log\alpha$. The DITs remain unchanged.
[20] L. N. Trefethen, *Spectral Methods in MATLAB* (SIAM, Philadelphia, 2000).
[21] R. A. Smith, Phys. Rev. Lett. **63**, 1479 (1989).
[22] S. Richardson, J. Fluid Mech. **102**, 263 (1981).
[23] B. Silverman, *Density Estimation for Statistics and Data Analysis* (Chapman and Hall, London, 1986).
[24] J. B. Weiss and J. C. McWilliams, Phys. Fluids A **3**, 835 (1991).
[25] T. L. Ashbee, J. G. Esler, and N. R. Mcdonald, J. Comput. Phys. **246**, 289 (2013); see the image model described therein. The equations are integrated using intervals $\Delta t = 0.1N$ time units and tolerance parameter $\delta = 10^{-8}$; see Eq. (6) of Ashbee *et al.* and surrounding discussion for details.
[26] L. M. Smith and V. Yakhot, Phys. Rev. Lett. **71**, 352 (1993).
[27] P.-H. Chavanis and J. Sommeria, J. Fluid Mech. **314**, 267 (1996).
[28] J. Miller, Phys. Rev. Lett. **65**, 2137 (1990).
[29] R. Robert, J. Stat. Phys. **65**, 531 (1991).
[30] R. Robert and J. Sommeria, J. Fluid Mech. **229**, 291 (1991).
[31] P.-H. Chavanis, Physica A **391**, 3657 (2012).
[32] M. T. DiBattista and A. J. Majda, Theor. Comput. Fluid Dyn. **14**, 293 (2001).